ADVANCED FUNCTIONAL MATERIALS
www.afm-journal.de

# Fiber-Reinforced Ultrathin Solid Polymer Electrolyte for Solid-State Lithium-Metal Batteries

*Yining Zhang, Jiameng Yu, Hongsheng Shi, Shuanghong Wang, Yinjie Lv, Yue Zhang, Qiong Yuan, Jinjiang Liang, Tianyi Gao, Ran Wei, Xin Chen, Luyao Wang, Yi Yu, and Wei Liu**

**Reducing the thickness of solid polymer electrolytes can help to enhance the energy density for solid-state batteries. However, ultrathin electrolytes still face difficulties in preparation methods, mechanical properties, and interface instability. Herein, a free-standing, scalable, and ultrathin solid polymer electrolyte with a thickness of 10 µm is reported. It is achieved through in situ thermal curing after filling a porous electrospun polyacrylonitrile fiber membrane with poly(ethylene glycol) diacrylate-based electrolyte. Impressively, it contributes to a high ionic conductivity of $8.8 \times 10^{-4}$ S cm$^{-1}$ at room temperature. The membrane can not only provide good mechanical strength but also offer a $Li_3N$-enriched solid electrolyte interphase, thereby stabilizing the lithium metal anode. The pouch cell pairing the ultrathin electrolyte with Li foil and $LiNi_{0.8}Co_{0.1}Mn_{0.1}O_2$ cathode of high mass loading can realize a gravimetric/volumetric energy density of 380 Wh kg$^{-1}$ and 936 Wh L$^{-1}$. This investigation provides new insights into the potential of fiber-reinforced membranes for high-performance solid-state batteries.**

## 1. Introduction

The demand for high-energy-density batteries continues to surge in parallel with the rapid development of portable electronic devices, electric vehicles, and grid-scale energy storage systems.[1] However, lithium-ion batteries (LIBs) would be difficult to meet these increasing requirements because of the restriction in energy density achievable imposed by intercalation chemistry and critical safety concerns.[2] Solid-state lithium-metal batteries (SSLMBs) are considered as next-generation energy storage systems due to their high potential for energy density and high safety.[3] When the thickness of the solid-state electrolyte (SSE) is reduced to less than 30 µm, the obtained battery is expected to exhibit a higher energy density exceeding 400 Wh kg$^{-1}$.[4] One of the most crucial difficulties in the pursuit of thin or ultrathin electrolytes is their mechanical strength, leading to safety and cycling lifespan issues.[5] In this regard, the fabrication of ultrathin electrolytes is of great importance.[6]

Typically, SSEs can be classified into inorganic solid electrolytes (ISEs) and solid polymer electrolytes (SPEs).[7] Although ISEs, especially garnets ($Li_7La_3Zr_2O_{12}$)[8] and perovskites ($Li_xLa_yTiO_3$),[9] show high ionic conductivity and Young's modulus,[10] their inherent brittleness and fragility aggravate challenges related to mechanical robustness and production of large size, ultrathin ISEs.[11] On the contrary, SPEs can reach the target thickness in terms of their high flexibility, excellent interface compatibility, and processability.[12] Nevertheless, low conductivity, electrochemical instability with high-voltage cathodes, and poor mechanical strength of ultrathin SPEs hinder their effective applications.[13] To address these issues, multiple researches to design high-performance SPEs have been conducted. One of the most efficient strategies is adding active fillers to construct composite solid electrolytes (CSEs).[14] The reinforcement fillers interacting with polymer segments can improve the ionic conductivity as well as mechanical and antioxidant performance, which have been widely studied.[15] Whereas, these additives, especially inorganic fillers, increase the overall weight and thickness and the complexity of fabrication.[16] Another strategy is introducing rigid and porous hosts into SPEs to enhance their mechanical integrity, which makes it easier to obtain ultrathin and lightweight SPEs.[17] To date, numerous investigations based on ultrathin SPEs have been developed extensively utilizing robust frameworks, including polyimide (PI),[18] polyethylene (PE),[19] cellulose[20] and polyvinylidene difluoride (PVDF)[21] coupled with a most studied system of polyoxyethylene oxide

Y. Zhang, J. Yu, H. Shi, S. Wang, Y. Lv, Y. Zhang, Q. Yuan, J. Liang, T. Gao, R. Wei, X. Chen, L. Wang, Y. Yu, W. Liu
School of Physical Science and Technology
ShanghaiTech University
Shanghai 201210, China
E-mail: liuwei1@shanghaitech.edu.cn
Y. Yu, W. Liu
Shanghai Key Laboratory of High-resolution Electron Microscopy
ShanghaiTech University
Shanghai 201210, China
W. Liu
Key Laboratory of Advanced Energy Materials Chemistry (Ministry of Education)
Nankai University
Tianjin 300071, China
The ORCID identification number(s) for the author(s) of this article can be found under https://doi.org/10.1002/adfm.202421054

DOI: 10.1002/adfm.202421054

 

(PEO)/lithium salt. For example, Cui's group prepared an ultrathin (28 µm) SPE of electrospun polyacrylonitrile (PAN) network and PEO/lithium salt, showing a stable interface and high thermal stability.[22] However, their electrochemical instability with high-voltage cathodes and limited Li-ion kinetics restrict the voltage elevation for higher energy-density cells.[23]

In this work, we constructed an ultrathin SPE combining an in situ thermal curing of poly(ethylene glycol) diacrylate (PEGDA) with an e-spun PAN fiber membrane. The ultrathin SPE (PAN fiber-PEGDA) with a thickness of 10 µm processed a superior ionic conductivity of $8.8 \times 10^{-4}$ S cm$^{-1}$ at room temperature. The e-spun PAN fiber framework was worked as a support to enhance the mechanical strength, hindering the propagation of lithium dendrite. Benefiting from the homogeneous $Li_3N$ enriched SEI, the Li|Li symmetrical batteries showed a long cycle lifespan with a low polarization. Additionally, the PAN fiber-PEGDA SPE exhibited a wider electrochemical window compared with the fiber-free SPE. The Li|$LiNi_{0.8}Co_{0.1}Mn_{0.1}O_2$ (NCM811) half cells using ultrathin SPE exhibited excellent rate performance and long cycle performance. Importantly, pouch cells based on 30 µm Li foil delivered a gravimetric/volumetric energy density of 380 Wh kg$^{-1}$ and 936 Wh L$^{-1}$.

## 2. Results and Discussion

### 2.1. Design of Ultrathin Electrolyte

In our previous work, PEGDA-based SPE was formed with succinonitrile (SN), lithium bis(trifluoromethanesulfonyl)imide (LiTFSI), and PEGDA polymer monomer, showing high ionic conductivity.[24] However, the mechanical and electrochemical properties of the PEGDA-based SPE need to be further improved, so the PAN fiber was introduced into this work. Here, we fabricated the ultrathin PAN fiber-PEGDA electrolyte through a two-step methodology. First, the PAN membrane was prepared by electrospinning, followed by calendaring to refine its structure (Figure S1, Supporting Information). Next, the precursor solution involving PEGDA monomer was filled into the PAN matrix for in situ thermal curing with lithium anode and cathode to assemble integrated full cells (**Figure 1a**). As shown in Figure S2 (Supporting Information), the cross-linked PEGDA electrolyte is composed of PEGDA monomer, SN-LiTFSI plastic crystal electrolyte, and fluoroethylene carbonate (FEC). Fluorinated additive FEC is added to stabilize the interface. The detailed preparation process of the SPEs is described in the experimental section of Supporting Information.

As illustrated in Figure 1a, when the PAN matrix is incorporated into the electrolyte as a host, the thickness of the free-standing solid electrolyte can be reduced to 10 µm due to the enhanced mechanical strength compared to the fiber-free one. The PAN fiber in the composite SPE facilitates anion trapping, then a higher Li-ion transference number can be obtained (Figure 1b). Besides, the PAN membrane can provide a more stable $Li_3N$-enriched SSE/Li interface, which enhances interfacial compatibility with the lithium anode. This enrichment effectively suppresses the growth of lithium dendrites (Figure 1c). Therefore, this ultrathin PAN fiber-PEGDA SPE enables both high energy density and safety in ASSLMBs.

### 2.2. Characterization of Ultrathin Electrolyte

To analyze the structural characteristics of the SPEs, scanning electron microscopy (SEM) images of the surface of the PAN membrane, PEGDA electrolyte, and PAN fiber-PEGDA electrolyte are shown in **Figure 2a–c**, respectively. The electrospun PAN nanofibers are porous and uniform (Figure 2a). The BET test demonstrates that the PAN membrane has numerous micropores with a surface area of 22.151 m$^2$ g$^{-1}$ (Figure S3, Supporting Information). The surface of the PEGDA electrolyte is flat and dense (Figure 2b), which is beneficial for interface contact. PAN fiber shows better wettability of the SN-based electrolyte precursor than commercial polyethylene (PE) separator (Figure S4a, Supporting Information) because PAN and SN have similar structures of C≡N.[25] PAN fiber (Figure 2a) also shows much higher porosity than the PE separator (Figure S4b, Supporting Information). The highly wettable and porous structure leads to a better uptake capacity of the precursor, which can improve the ionic conductivity. The PAN membrane turns from white into transparent after the precursor solution is infused. Figure 2c suggests that the PEGDA polymer can uniformly fill into the pores of the PAN network. The cross-sectional SEM image (Figure 2d) shows that the thickness of the PAN fiber-PEGDA electrolyte is as thin as 10 µm. The corresponding energy dispersive spectroscopy (EDS) mappings are displayed in Figure 2e, demonstrating the even distribution of PAN fiber-PEGDA electrolyte in composition. Meanwhile, the weight of the ultrathin electrolyte is only 1.8 mg cm$^{-2}$.

The SPEs were achieved by in situ thermal curing after mixing the precursor solution (Figure 2f). The Fourier transformation infrared (FT-IR) spectra were carried out to elucidate the cross-linking of the polymer monomer. As depicted in Figure 2g, the stretching vibration of C═C (at 1600–1650 cm$^{-1}$) peak in PEGDA monomer is absent after thermal treatment, confirming the polymerization of the precursor solution. From the enlarged views of FT-IR spectra (Figure S5, Supporting Information), the peak of C═O (1724 cm$^{-1}$) in polymer monomer and the peak of $CH_2$ (1427 cm$^{-1}$) in the SN electrolyte remain unchanged in both PEGDA and PAN fiber-PEGDA electrolyte. It can be inferred that the thermal polymerization process does not trigger any side reactions. The plastic crystal behavior of the SPEs was characterized by differential scanning calorimetry (DSC) analysis. The two SPEs show two peaks corresponding to the transition temperature from crystal to plastic crystal phase ($T_{cp}$) and the melting temperature of SN ($T_m$).[26] As shown in Figure 2h, both of them appear similar $T_{cp}$, demonstrating that the plastic crystal behavior is not broken with the addition of PAN membrane. And the $T_m$ increases from 19 °C (PEGDA electrolyte) to 24 °C (PAN fiber-PEGDA electrolyte). Although the increased $T_m$ leads to fewer structural defects in SN, such as trans-gauche, which sightly limits its ionic mobility,[27] it ensures that the electrolyte remains in a solid state at room temperature.

Then, the SPEs were exposed to various temperatures (50, 80, 100, and 120 °C) on the hotplate to evaluate their thermal stability. As illustrated in Figure S6 (Supporting Information), when the temperature is elevated to 120 °C, PEGDA electrolyte shows obvious cracks. By contrast, PAN fiber-PEGDA electrolyte shows no significant changes in its structure and still retains its excellent flexibility. The thermogravimetric analysis (TGA) curves also

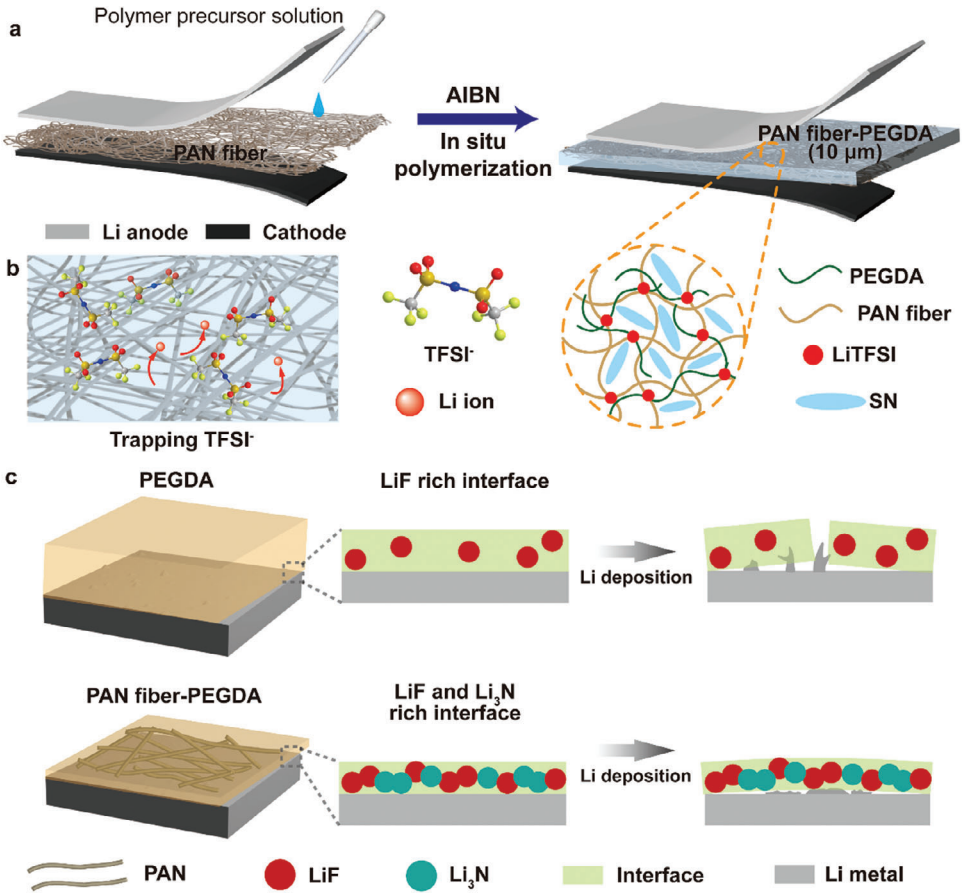


**Figure 1.** Schematic illustration of the ultrathin PAN fiber-PEGDA solid polymer electrolyte. a) The synthesis process of this electrolyte. PAN fiber can b) facilitate $Li^+$ ion transportation, c) improve dendrite resistance and interfacial compatibility for lithium metal batteries.

reveal that the SPEs have good thermal stability, with obvious weight loss at 130 °C, signifying the thermal decomposition of SN (Figure S7, Supporting Information). Additionally, the mechanical property is an important criterion for SPEs in their practical use. The stress–strain test results of the two SPEs are shown in Figure 2i. The PAN fiber-PEGDA electrolyte displays a significant improvement in both tensile strength and elongation (5.62 MPa and 54%) compared to the PEGDA electrolyte. Its modulus is ≈100 MPa, which is over 100 times higher than the modulus of PEGDA. The enhanced thermal stability and mechanical properties of PAN fiber-PEGDA electrolyte are owed to the robust PAN matrix, inducing it to be a promising SPE for ASSLMBs.

### 2.3. Electrochemical Performances of Ultrathin Electrolyte

Various electrochemical tests were carried out to analyze the performance of the ultrathin electrolyte. According to the electrochemical impedance spectroscopy (EIS) result (Figure S8, Supporting Information), the ionic conductivity of PEGDA electrolyte is calculated to be $9.8 \times 10^{-4}$ S cm$^{-1}$ at room temperature. With the introduction of PEGDA electrolyte permeating into the PAN membrane, PAN fiber-PEGDA can also reach a high ionic conductivity ($8.8 \times 10^{-4}$ S cm$^{-1}$). Although PEGDA electrolyte has a higher ionic conductivity, its poor mechanical strength restricts the thickness of the electrolyte (PEGDA over 700 μm, Figure S9, Supporting Information). When the thickness of the PEGDA SPE is reduced, it can hardly keep the original configuration without the support of reinforced frameworks. Apart from ionic conductivity, the ionic conductance is of equal importance because the thickness of SPEs is taken into consideration.[28] The ionic conductance of PAN fiber-PEGDA is 0.1 S, which is much higher than that of PEGDA (0.017 S). A higher ionic conductance brings about shorter Li ion diffusion time across SSEs, which is of great significance for high energy density SSLMBs.

The temperature dependence of ionic conductivity for PAN fiber-PEGDA electrolyte was also evaluated over a range of temperatures from 10 to 80 °C (Figure S10, Supporting Information). As shown in **Figure 3a**, the activation energy ($E_a$) is measured to be 0.35 eV, which is lower than the reported PEGDA-based electrolytes.[29] The PAN fiber-PEGDA electrolyte shows lower kinetic energy barriers for Li-ion transportation. The linear sweep voltammetry (LSV) curves were studied to evaluate their oxidation ability with cathodes in Figure 3b. It is revealed that the electrochemical window of PAN fiber-PEGDA electrolyte is elevated to 4.8 V in comparison to that of PEGDA (4.3 V). This can be attributed to the high-voltage tolerance of PAN from its strong electron absorption ability of the C≡N polar group.[30] The electrochemical floating tests of Li|SPE|NCM811 cells were further explored (Figure 3c). The leakage current of PAN fiber-PEGDA

 

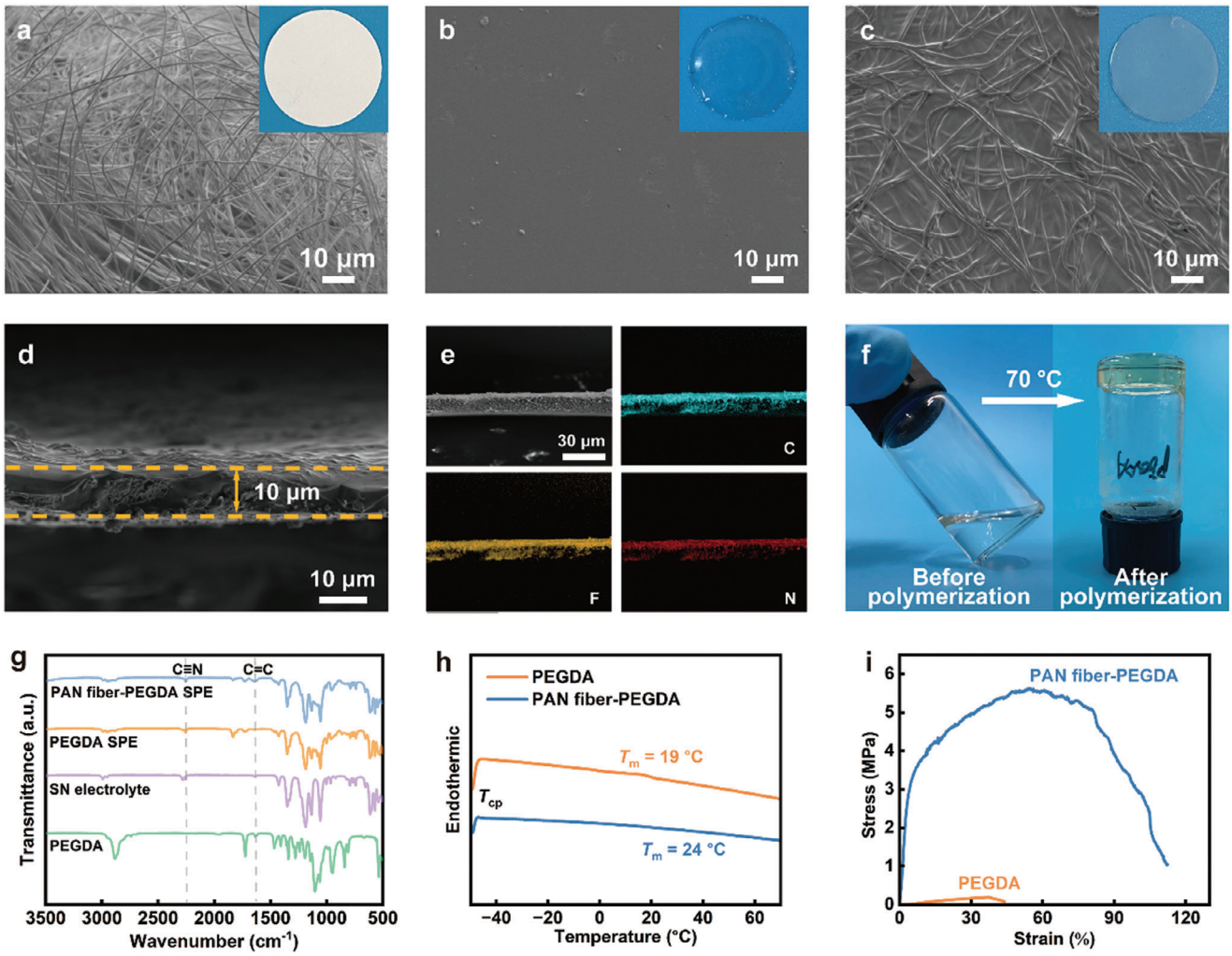


**Figure 2.** Characterization of the ultrathin solid polymer electrolyte. SEM image from the top view of a) PAN fibers, b) PEGDA film, and c) PAN fiber-PEGDA film. (insets show optical photos of them respectively). d) Cross-sectional SEM images of PAN fiber-PEGDA. e) EDS mapping of PAN fiber-PEGDA. f) Digital images of the PEGDA precursor solution (left) and corresponding polymer after thermal curing (right). g) The FT-IR spectra of the PEGDA monomer, SN electrolyte, PEGDA, and PAN fiber-PEGDA. h) DSC curves and i) Stress–strain curves of the PEGDA and PAN fiber-PEGDA.

is stable between 4.0 and 4.6 V, while the current of the PEGDA cell fluctuates at the voltage of 4.4 V. These results further elucidate that the addition of PAN fiber enhances the electrochemical stability of the SPE.

In addition, the PAN fiber-PEGDA electrolyte exhibits a higher $Li^+$ transference number ($t_{Li}^+$) of 0.42 than that of PEGDA for only 0.19 (Figure 3d,e). A higher $t_{Li}^+$ can reduce the interfacial polarization and promote a more homogeneous distribution of lithium deposition.[31] The C≡N groups of PAN chains can adsorb $TFSI^-$ and facilitate the dissociation of lithium salts,[32] which results in a higher $t_{Li}^+$. This is also confirmed by the Raman spectroscopy (Figure 3f) and FT-IR spectra (Figure S11, Supporting Information). The Raman spectra show the N—S bonds stretching vibrations of $TFSI^-$ in different SPEs.[33] This peak can be divided into the peak of free anions at ≈741 $cm^{-1}$ and the peak of fixed anions at ≈745 $cm^{-1}$.[34] After the Gaussian-Lorentzian fitting, the ratio of fixed $TFSI^-$ increases from 24.31% in the electrolyte without PAN to 34.17% in that with PAN fiber (Table S1, Supporting Information). The increased ratio of fixed $TFSI^-$ can be also affirmed by FT-IR spectra. The $TFSI^-$ peak for PAN fiber-PEGDA electrolyte exhibits a higher wavenumber, inferring a higher ratio of fixed $TFSI^-$[35] (Figure S11, Supporting Information). These results indicate that part of the anions are immobilized by the PAN chains, which can successfully diminish the interfacial polarization.

To further confirm the interactions between polymer chains and Li salt, density functional theory (DFT) calculations were conducted. The optimized atomic model depicted in Figure 3g demonstrates that the $TFSI^-$ anions tend to be drawn on the C≡N groups on the PAN chains. As illustrated in Figure 3h, the adsorption energy between PAN and $TFSI^-$ is −1.34 eV, which is obviously lower than that between PEGDA and $TFSI^-$ (−0.76 eV). This suggests that the $TFSI^-$ anions are anchored by the C≡N groups on PAN chains, which results in more removable Li ions in the electrolyte, consequently boosting a higher $t_{Li}^+$. The DFT results also agree with the Raman spectra presented in Figure 3f.

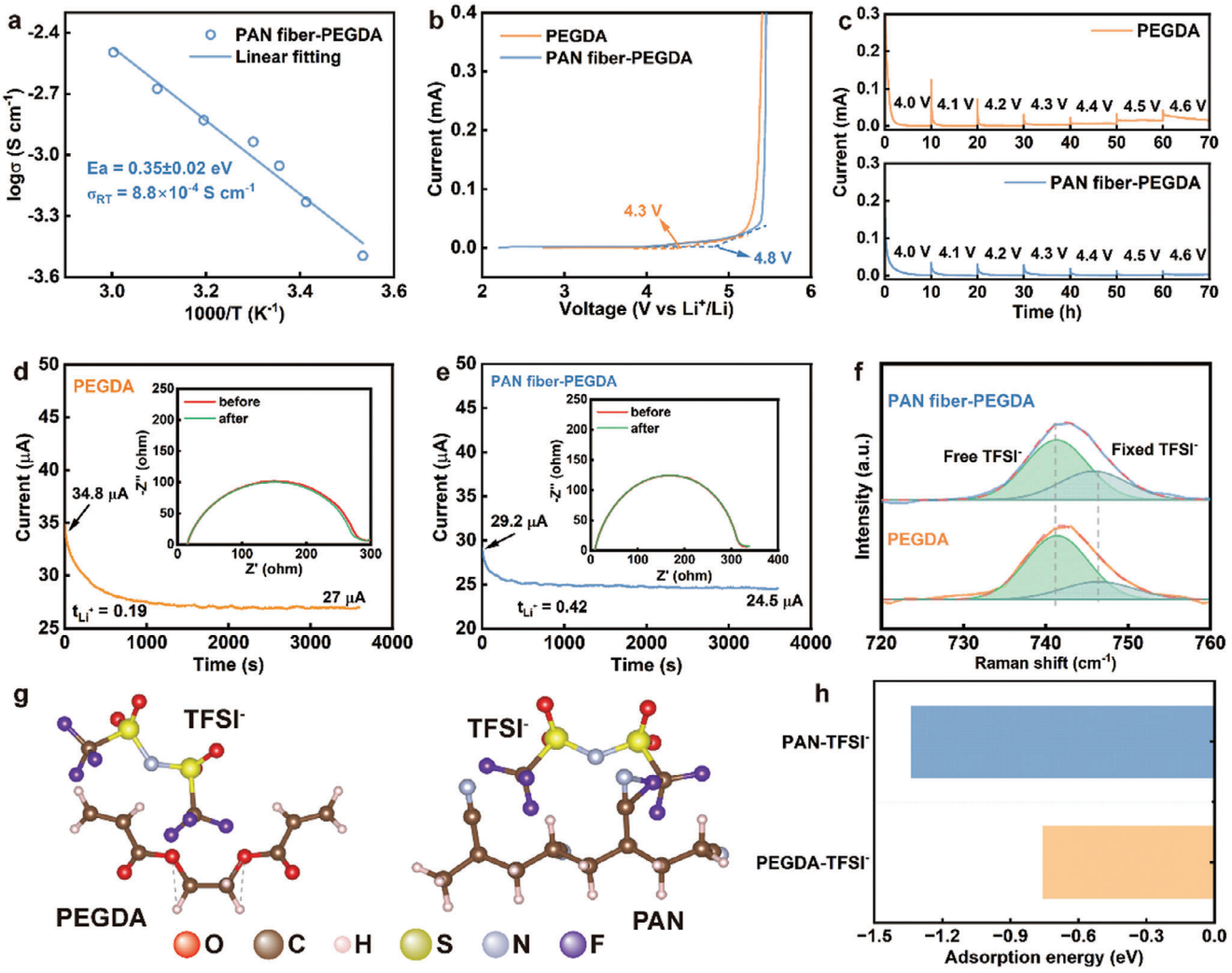


**Figure 3.** Electrochemical performance of the ultrathin solid polymer electrolyte. a) The Arrhenius plots of PAN fiber-PEGDA polymer electrolyte. b) LSV curves of PEGDA and PAN fiber-PEGDA electrolyte. c) Electrochemical floating analysis of cells assembled with NCM811 cathode for PEGDA and PAN fiber-PEGDA electrolyte. Chronoamperometry curves with a step voltage of 10 mV for d) PEGDA, e) PAN fiber-PEGDA electrolyte (insets displayed EIS plot before and after polarization). f) Raman spectra for PEGDA and PAN fiber-PEGDA electrolyte. g) Optimized atomic model of the dissociated $TFSI^-$ adsorbed on the surface of PEGDA and PAN, respectively. h) Adsorption energy of the $TFSI^-$ on PEGDA and PAN.

### 2.4. Li Metal Anode Stability of Ultrathin Electrolyte

Lithium symmetric batteries are used to study the stability of the SPEs with lithium metal anode. As illustrated in Figure S12 (Supporting Information), the PAN fiber-PEGDA electrolyte shows lower interfacial impedance than the PEGDA electrolyte during cycling, indicating its better interfacial affinity for lithium metal. Besides, the critical current density is a critical merit to evaluate the inhibition ability of SEs to lithium dendrite growth.[36] The CCD of PAN fiber-PEGDA is 1.04 mA $cm^{-2}$, which is higher than the PEGDA electrolyte of 0.60 mA $cm^{-2}$ (**Figure 4a**). It can be mainly attributed to the efficient transport of Li ions at the interface and improved mechanical strength. The Li plating/stripping behavior was carried out ranging from 0.05 to 0.5 mA $cm^{-2}$, and then to 0.1 mA $cm^{-2}$ (Figure 4b). The Li|PAN fiber-PEGDA|Li cell can cycle stably up to a current density of 0.5 mA $cm^{-2}$ without a short circuit and it maintains stable cycling performance for 3000 h at 0.1 mA $cm^{-2}$ (Figure S13, Supporting Information). In contrast, the Li|PEGDA|Li cell occurs a short circuit when the current density is elevated to 0.4 mA $cm^{-2}$. Then Figure 4c shows the periodically charged and discharged curves at a current density of 0.2 mA $cm^{-2}$. The electrolyte with PAN fiber maintains a steady running with a polarization of 45 mV after 600 h cycling, which is superior to that of PEGDA electrolyte with only 75 h cycling.

To elucidate the impact of PAN fiber on the evolution of the Li|SPE interface, a COMSOL simulation was carried out. The comprehensive methodologies and parameters used are detailed in Table S2 (Supporting Information). As illustrated in Figure 4d, e, in contrast to PEGDA electrolyte, PAN fiber-PEGDA demonstrates a notably uniform Li-ion distribution and reduced potential distribution because of the improved Li-ion transference number. Smaller concentration polarization results in uniform lithium deposition, thereby enhancing the long cycling performance.

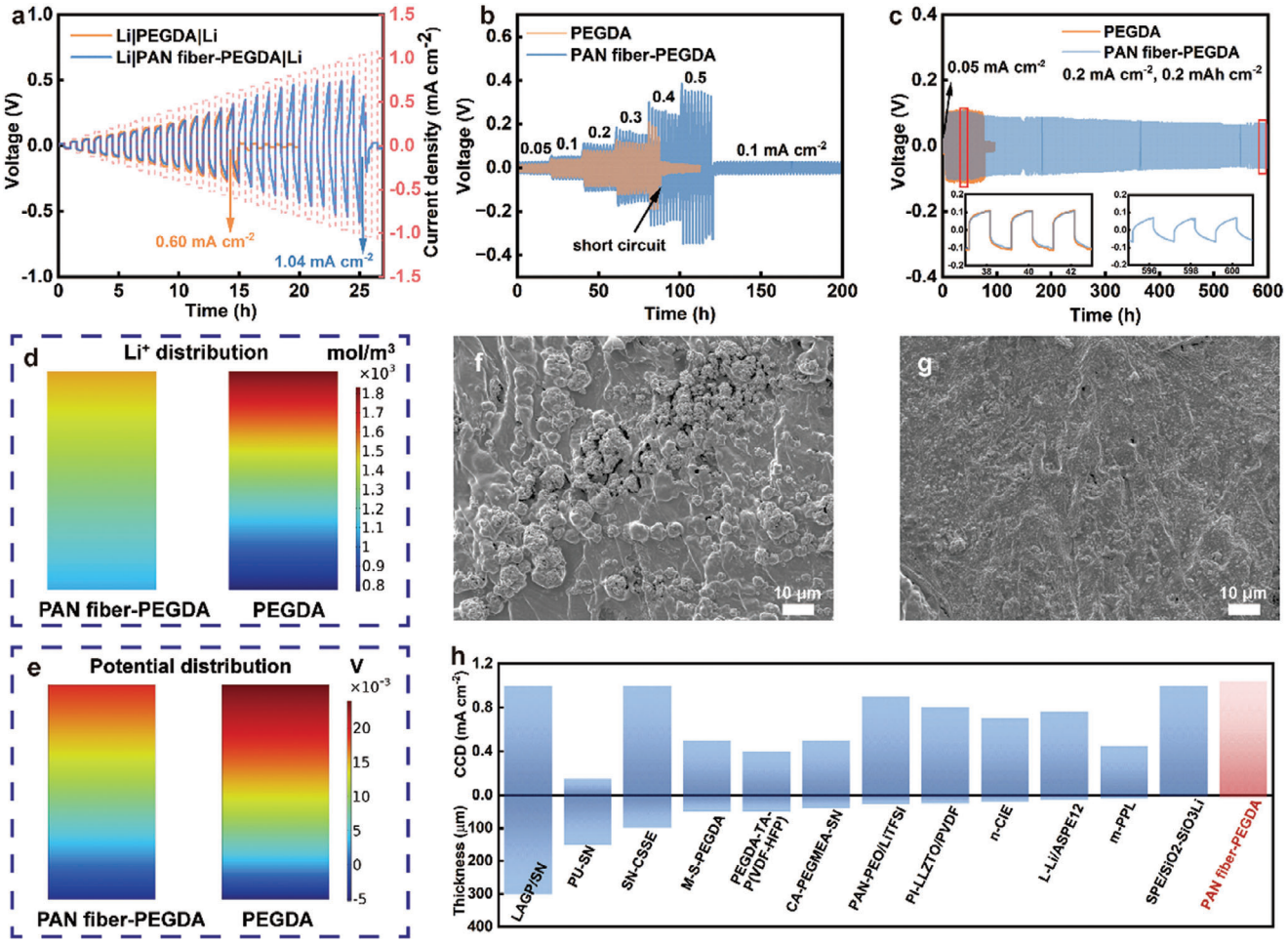


**Figure 4.** Electrochemical performance of Li symmetric batteries. a) The critical current density of PEGDA and PAN fiber-PEGDA electrolyte. Galvanostatic cycling performance of Li|Li symmetrical cells b) under various current densities from 0.05 to 0.5 mA cm$^{-2}$ and c) at 0.2 mA cm$^{-2}$, 0.2 mAh cm$^{-2}$ at room temperature. Simulation of d) Li-ion concentration gradient and e) potential distribution in symmetric cells of PEGDA and PAN fiber-PEGDA electrolyte. SEM images of the lithium metal surface of f) Li|PEGDA|Li cell cycling after 50 h and g) Li|PAN fiber-PEGDA|Li cell cycling after 300 h. h) Comparison of the CCD based on the thickness for our work with reported SSEs.

Furthermore, to understand the enhancement of interface stability between the electrolyte and lithium metal anode, top-view SEM images of the lithium anode from disassembled Li symmetric cells after cycling are shown in Figure 4f,g. It is distinct that uneven lithium deposition and mossy dendrites can be found on the surface of the lithium metal for Li|PEGDA|Li cell after cycling 50 h (Figure 4f). On the contrary, the morphology of the lithium anode for PAN fiber-PEGDA cell is rather flat and smooth without dendrites (Figure 4g). This demonstrates that applying the PAN matrix in the electrolyte can effectively homogenize the lithium deposition. These experimental outcomes indicate that PAN fiber-PEGDA can achieve a dendrite-free surface on the lithium anode after long-term cycling, which corresponds with the above-mentioned simulation results. Therefore, PAN fiber-PEGDA allows for uniform lithium plating/stripping, guaranteeing a competitive CCD and corresponding thickness, which is compared with various SPEs and CSEs reported in the literature (Figure 4h; Table S3, Supporting Information).[22,37]

Then, the structure and composition of the solid electrolyte interphase (SEI) of Li|SPE interface after 50 h of cycling at different etching durations were investigated by transmission electron microscopy (TEM) and X-ray photoelectron spectroscopy (XPS) tests. The SEI formed by PAN fiber-PEGDA electrolyte possesses a more uniform and thinner thickness (Figure S14a, Supporting Information). In contrast, PEGDA electrolyte exhibits an uneven SEI with a thickness of ≈20 nm (Figure S14b, Supporting Information). For the compositional analysis, as shown in **Figure 5a**, the peaks of F 1s are assigned to be Li-F (684.8 eV) and C-F (688.6 eV). Based on the XPS spectra with different etching times, an increase in LiF (from 21.9% to 96.2%) and a concurrent decrease in organic components were detected with increasing sputtering depth in the SEI for PAN fiber-PEGDA electrolyte (Figure 5b). Li|PAN fiber-PEGDA|Li cell reveals a much higher content of LiF (up to over 96%), suggesting the formation of a denser and more uniformly distributed SEI, compared to that of PEGDA electrolyte.

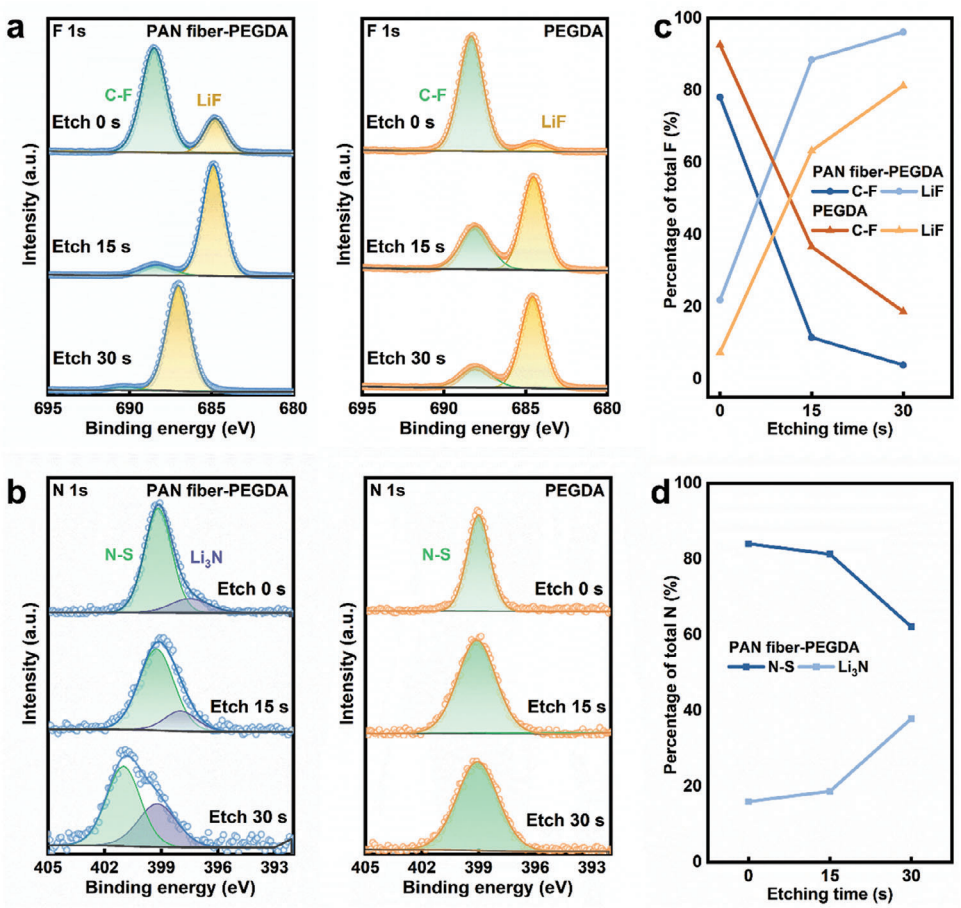


**Figure 5.** XPS spectra with depth profiles of lithium anode with PEGDA and PAN fiber-PEGDA electrolyte after 50 h of cycling: a) F 1s and b) N 1s. The calculated composition ratio of the solid electrolyte interphase (SEI) for c) F and d) N.

Moreover, the N 1s spectrum shows two peaks at 399.2 eV and 397.1 eV corresponding to LiTFSI and $Li_3N$ (Figure 5c). A significant Li-N signal is found in the SEI of Li|PAN fiber-PEGDA interface while no obvious $Li_3N$ appears in the interface for PAN-free PEGDA electrolyte. In addition, as depicted in Figure 5d, the content of $Li_3N$ increases from 16% to 38% during the sputtering process coming from the PAN membrane. The existence of more $Li_3N$ can further eliminate uneven current distribution because $Li_3N$ is a superionic $Li^+$ conductor,[38] benefiting ion transport at the interface.[39] Therefore, more abundant inorganic composition (LiF), which arises from the decomposition of LiTFSI and FEC additive in the SEI of PAN fiber-PEGDA, effectively facilitates uniform lithium deposition and hinders the formation of lithium dendrite. The coexistence of $Li_3N$ in the SEI ensures remarkable interfacial stability of PAN fiber-PEGDA with lithium anode during long cycling periods.

### 2.5. Performance of Ultrathin Electrolyte-Based Lithium Metal Batteries

In situ polymerization strategy can successfully improve the electrode/electrolyte interface contact.[40] The feasibility of this in situ fabricated ultrathin electrolyte in practical applications was evaluated by Li||$LiFePO_4$ (LFP) and Li||NCM811 half cells at room temperature. As illustrated in **Figures** 6a and S15 (Supporting Information), the homogeneous prepolymer solution can be effectively filled into pores within the cathode, forming a tight contact interface. The cross-section SEM image of electrolyte/NCM811 cathode with a high mass loading of 8 mg $cm^{-2}$ is presented in Figure 6b with its corresponding energy-dispersive spectroscopy (EDS) in Figure 6c. A higher magnification SEM image of the cathode is shown in Figure 6d. These results demonstrate that the precursor components can penetrate well into the high-mass loading cathode, realizing seamless solid–solid contact.

Figure 6e,f shows the rate performance of the Li||LFP cells as the current densities increased from 0.1 to 0.5 C. The PAN fiber-PEGDA delivers specific capacities of 155.6, 152.2, 147.4, 141.8, and 136.4 mAh $g^{-1}$ at 0.1, 0.2, 0.3, 0.4, and 0.5 C, respectively. Notably, when the current density returns to 0.1 C, the specific capacity can be recovered to 155.2 mAh $g^{-1}$, which is similar to the original capacity of 0.1 C. Their cycling performance were also tested over a voltage range of 2.5–4.0 V at 0.3 C. Figure 6g reveals that Li|PAN fiber-PEGDA|LFP cell exhibits an initial discharge capacity of 143.1 mAh $g^{-1}$ at 0.3 C and retains a discharge capacity of 125.5 mAh $g^{-1}$ after 145 cycles with a high capacity retention of ≈88%. The galvanostatic charge–discharge curves of Li||LFP cells at 0.3 C during different cycles are shown in Figure S16 (Supporting Information). Conversely, the Li|PEGDA|LFP cell shows

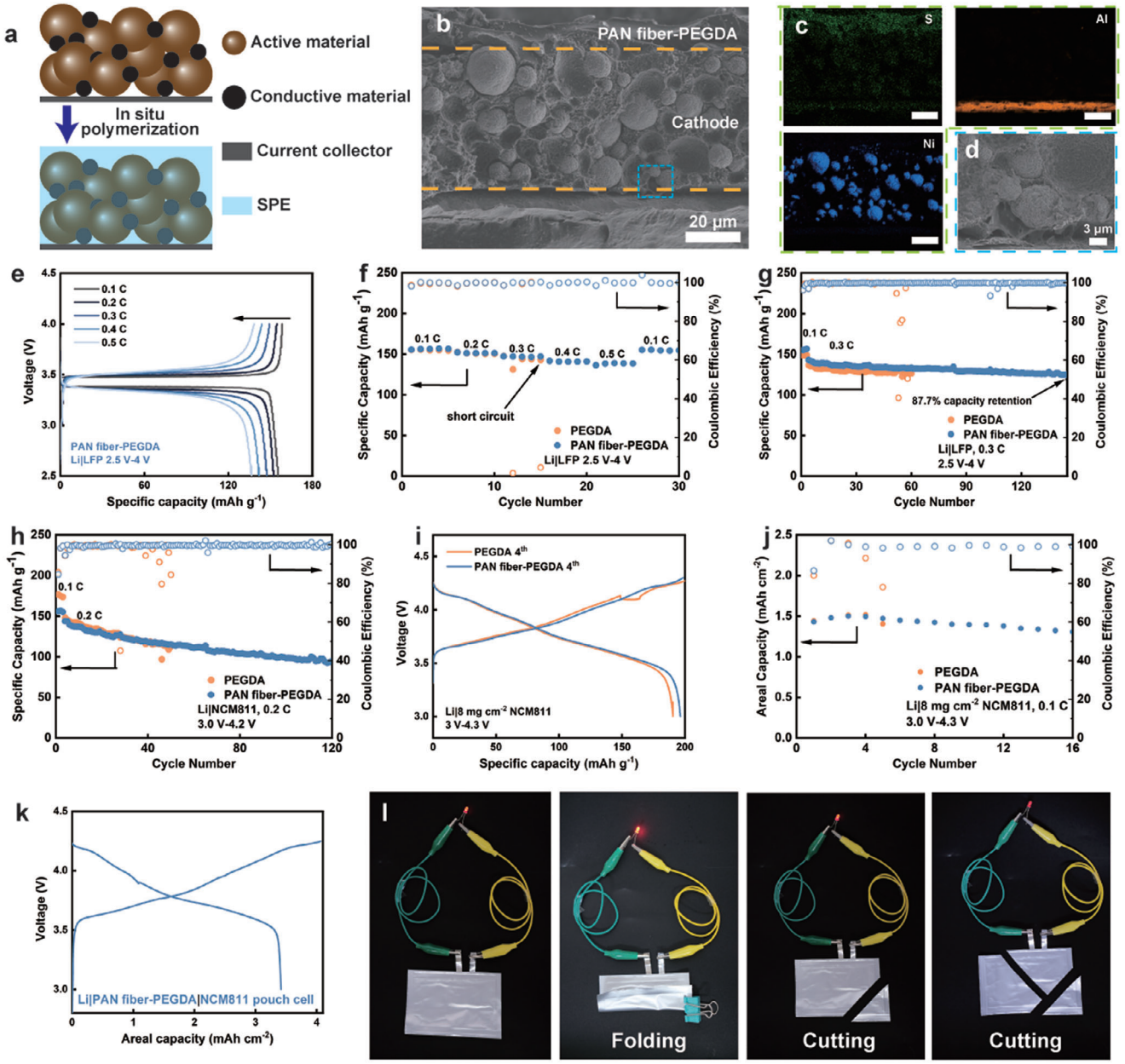


**Figure 6.** Performance half-cell batteries. a) Schematic diagram showing the in situ fabricating of SPE in cells. b) Cross-sectional SEM images of PAN fiber-PEGDA and NCM811. c) Magnified cross-sectional SEM image of b). d) Corresponding ESD mapping of Al, Ni, and S elements. e) Charge and discharge curves of Li|PAN fiber-PEGDA|LFP half cell at different rates. f) Rate performance of Li||LFP half cell from 0.1 to 0.5 C. g) Cycle stability of Li||LFP at 0.3 C. h) Cycling stability of Li||NCM811 half cell at 0.2 C. i) Charge and discharge curves at 4th cycle, j) cycle stability of Li||NCM811 with high mass loading 8 mg $cm^{-2}$. k) Charge and discharge curves of Li|PAN fiber-PEGDA|NCM811 pouch cell. l) An LED is powered by the pouch cell under folding and cutting.

a short circuit after only 55 cycles (Figure S16b, Supporting Information).

Furthermore, to assess the compatibility and practical potential of the ultrathin electrolyte with high-voltage cathodes, Li|SPE|NCM811 cell configurations were assembled and tested. The PAN fiber-PEGDA presents a much better rate capability than that of PEGDA electrolyte in Li||NCM811 cells (Figure S17, Supporting Information). The long cycling performances are shown in Figure 6h with the cut-off voltage of 4.2 V at 0.2 C. The initial capacity of the PAN fiber-PEGDA electrolyte is 139.5 mAh $g^{-1}$, yielding a capacity retention of 70% after 120 cycles. Figure S18 (Supporting Information) illustrates the evolution of charge/discharge profiles of PAN fiber-PEGDA and PEGDA electrolyte. Similarly, the Li|PEGDA|NCM811 occurs in a short circuit after 46 cycles (Figure S18b, Supporting Information). These results manifest that the presence of PAN fiber in the electrolyte convinces reliability in the cycle lifespan and avoids the growth of lithium dendrites.

Meanwhile, cells with a high mass loading of about 8 mg $cm^{-2}$ NCM811 cathode were also assembled. As shown in Figure 6i, when the Li||NCM811 cells are operated with the range to a higher voltage of 4.3 V at 0.1 C, the charge curve of the PEGDA electrolyte displays an obvious fluctuation during the 4th cycle. In contrast, in Figure 6j and Figure S19 (Supporting Information), the Li|PAN fiber-PEGDA|NCM811 cells could deliver a high area capacity ≈1.43 mAh $cm^{-2}$, indicating that the PAN membrane can improve the high voltage compatibility of the SPE. Then, the cathodes NCM811 with $LiNbO_3$ coating were assembled in half cells. Even when the cut-off voltage was increased to 4.5 V, Li|PAN fiber-PEGDA|NCM811@$LiNbO_3$ half cell exhibits a high initial capacity of 170.4 mAh $g^{-1}$ with capacity retention of 73% after 40 cycles (Figure S20, Supporting Information). Therefore, PAN fiber-PEGDA electrolyte affords better cycling performance, particularly under elevated cut-off voltage or with higher mass loading cathodes.

Leveraging these advantages, the practical application of the ultrathin electrolyte in full batteries was further evaluated in the Li|PAN fiber-PEGDA|NCM811 pouch cells. The pouch cell pairing with high mass loading NCM811 cathode (20.3 mg $cm^{-2}$) and thin lithium foil anode (30 µm) was assembled. As shown in Figure 6k, the high area capacity can achieve 3.42 mAh $cm^{-2}$ at charge cut-off voltages of 4.25 V and remain 3.20 mAh $cm^{-2}$ after 6 cycles. In contrast, Li|PEGDA|NCM811 (20.3 mg $cm^{-2}$) cell can only reach a specific capacity of 88.9 mAh $g^{-1}$ (Figure S21, Supporting Information). The gravimetric/volumetric energy density of this pouch cell can even reach 380 Wh $kg^{-1}$ and 936 Wh $L^{-1}$ (the detailed calculation is shown in Table S4, Supporting Information). Additionally, the pouch cell can effectively power the light-emitting diode (LED) even under conditions of folding and cutting (Figure 6l). Therefore, the PAN fiber-PEGDA electrolyte possesses good safety and reliability for practical high-energy-density batteries.

## 3. Conclusion

In summary, we presented an ultrathin SPE (10 µm) by in situ thermal curing PEGDA with PAN fibers-reinforced. With the help of cross-linked PEGDA polymer electrolyte, the room temperature ionic conductivity of PAN fiber-PEGDA could achieve $8.8 \times 10^{-4}$ S $cm^{-1}$. Meanwhile, the PAN matrix could provide a good mechanical strength. The critical current density of the PAN-PEGDA achieved 1.04 mA $cm^{-2}$. The PAN fiber-PEGDA electrolyte also enabled even and smooth lithium deposition and excellent lithium compatibility a $Li_3N$-enriched SSE/Li interface, inhibiting the growth of lithium dendrites. The symmetrical Li|Li cells delivered more than 600 h at 0.2 mA $cm^{-2}$ without a short circuit. Furthermore, the full pouch battery based on this ultrathin SPE reached an impressive energy density of 380 Wh $kg^{-1}$. This investigation provides a new insight into the potential of fiber-reinforced SPEs for the practical assembly of high energy density ASSLMBs.

## Supporting Information

Supporting Information is available from the Wiley Online Library or from the author.

## Acknowledgements

The authors gratefully acknowledge financial support from the National Natural Science Foundation of China (92472119, 52222311), the Natural Science Foundation of Shanghai (24ZR1451200), and Double First-Class Initiative Fund of ShanghaiTech University. The microscopy experiments were supported by the Center for High-resolution Electron Microscopy (CħEM) at ShanghaiTech University.

## Conflict of Interest

The authors declare no conflict of interest.

## Data Availability Statement

The data that support the findings of this study are available from the corresponding author upon reasonable request.

## Keywords

fibres, interface stability, lithium-metal batteries, solid polymer electrolyte, ultrathin

Received: November 1, 2024
Revised: January 15, 2025
Published online: January 29, 2025

[1] a) W. Liu, W. Pan, J. Luo, A. Godfrey, G. Ou, H. Wu, W. Zhang, *Nat. Commun.* **2015**, *6*, 8354; b) P. Lennartz, B. A. Paren, A. Herzog-Arbeitman, X. C. Chen, J. A. Johnson, M. Winter, Y. Shao-Horn, G. Brunklaus, *Joule* **2023**, *7*, 1471; c) Y. Guo, S. Wu, Y.-B. He, F. Kang, L. Chen, H. Li, Q.-H. Yang, *eScience* **2022**, *2*, 138; d) Y. Jie, C. Tang, Y. Xu, Y. Guo, W. Li, Y. Chen, H. Jia, J. Zhang, M. Yang, R. Cao, Y. Lu, J. Cho, S. Jiao, *Angew. Chem., Int. Ed.* **2024**, *63*, 202307802; e) W.-h. Hou, Y. Lu, Y. Ou, P. Zhou, S. Yan, X. He, X. Geng, K. Liu, *Trans. Tianjin Univ.* **2023**, *29*, 120.

[2] W. Gu, G. Xue, Q. Dong, R. Yi, Y. Mao, L. Zheng, H. Zhang, X. Fan, Y. Shen, L. Chen, *eScience* **2022**, *2*, 486.

[3] a) S. Xia, X. Wu, Z. Zhang, Y. Cui, W. Liu, *Chem* **2019**, *5*, 753; b) Q.-K. Zhang, X.-Q. Zhang, J. Wan, N. Yao, T.-L. Song, J. Xie, L.-P. Hou, M.-Y. Zhou, X. Chen, B.-Q. Li, R. Wen, H.-J. Peng, Q. Zhang, J.-Q. Huang, *Nat. Energy* **2023**, *8*, 725.

[4] a) Q. Zhang, J. Zhou, P. Cui, Z. Wang, P. Lv, K. Yu, W. Wei, *J. Mater. Chem. A* **2023**, *11*, 15122; b) X. Yang, K. R. Adair, X. Gao, X. Sun, *Energy Environ. Sci.* **2021**, *14*, 643.

[5] a) M. Sun, Z. Zeng, L. Peng, Z. Han, C. Yu, S. Cheng, J. Xie, *Mater. Today Energy* **2021**, *21*, 100785; b) J. Feng, J. Wang, Q. Gu, W. Thitisomboon, D. Yao, Y. Deng, P. Gao, *J. Mater. Chem. A* **2022**, *10*, 13969.

[6] X. Lu, Y. Wang, X. Xu, B. Yan, T. Wu, L. Lu, *Adv. Energy Mater.* **2023**, *13*, 2301746.

[7] Y.-W. Song, S.-J. Park, H. Lee, M.-Y. Kim, H.-S. Kim, S.-W. Kang, S. Lee, Y. Kim, J. Kim, J. Lim, *J. Mater. Chem. A* **2024**, https://doi.org/10.1039/D4TA00479E.

[8] Y. Zhang, W. Zhai, X. Hu, Y. Jiang, S. Chen, Y. Zhang, W. Liu, Y. Yu, *Nano Res.* **2023**, *16*, 4039.

[9] Y. Zhang, S. Chen, Y. Zhang, Y. Yu, W. Liu, *Appl. Phys. Lett.* **2022**, *121*, 173903.

[10] a) C. Zhang, X. Hu, Z. Nie, C. Wu, N. Zheng, S. Chen, Y. Yang, R. Wei, J. Yu, N. Yang, Y. Yu, W. Liu, *J. Adv. Ceram.* **2022**, *11*, 1530; b) X. Yi, Y. Guo, S. Pan, Y. Wang, S. Chi, S. Wu, Q.-H. Yang, *Trans. Tianjin Univ.* **2023**, *29*, 73.

 

[11] a) M. Balaish, J. C. Gonzalez-Rosillo, K. J. Kim, Y. Zhu, Z. D. Hood, J. L. M. Rupp, *Nat. Energy* **2021**, *6*, 227; b) C. Bao, C. Zheng, M. Wu, Y. Zhang, J. Jin, H. Chen, Z. Wen, *Adv. Energy Mater.* **2023**, *13*, 2204028.
[12] a) W. Liu, S. W. Lee, D. Lin, F. Shi, S. Wang, A. D. Sendek, Y. Cui, *Nat. Energy* **2017**, *2*, 17035; b) L. Nie, S. Chen, M. Zhang, T. Gao, Y. Zhang, R. Wei, Y. Zhang, W. Liu, *Nano Res.* **2024**, *17*, 2687.
[13] a) J. Yu, Y. Zhang, T. Gao, X. Zhang, Y. Lv, Y. Zhang, C. Zhang, W. Liu, *Chem. Eng. J.* **2024**, *487*, 150646; b) Q. Wang, S. Wang, T. Lu, L. Guan, L. Hou, H. Du, H. Wei, X. Liu, Y. Wei, H. Zhou, *Adv. Sci.* **2023**, *10*, 2205233.
[14] Q. Hu, Z. Sun, L. Nie, S. Chen, J. Yu, W. Liu, *Mater. Today Energy* **2022**, *27*, 101052.
[15] a) W. Liu, N. Liu, J. Sun, P.-C. Hsu, Y. Li, H.-W. Lee, Y. Cui, *Nano Lett.* **2015**, *15*, 2740; b) F. He, W. Tang, X. Zhang, L. Deng, J. Luo, *Adv. Mater.* **2021**, *33*, 2105329.
[16] L. Liu, Y. Shi, M. Liu, Q. Zhong, Y. Chen, B. Li, Z. Li, T. Zhang, H. Su, J. Peng, N. Yang, P. Wang, A. Fisher, J. Niu, F. Wang, *Adv. Funct. Mater.* **2024**, *n/a*, 2403154.
[17] M. Zhang, H. Wang, A. Shao, Z. Wang, X. Tang, S. Li, J. Liu, Y. Ma, *Adv. Energy Mater.* **2024**, *14*, 2303932.
[18] J. Wan, J. Xie, X. Kong, Z. Liu, K. Liu, F. Shi, A. Pei, H. Chen, W. Chen, J. Chen, X. Zhang, L. Zong, J. Wang, L.-Q. Chen, J. Qin, Y. Cui, *Nat. Nanotechnol.* **2019**, *14*, 705.
[19] J. Wu, Z. Rao, Z. Cheng, L. Yuan, Z. Li, Y. Huang, *Adv. Energy Mater.* **2019**, *9*, 1902767.
[20] C. Yang, Q. Wu, W. Xie, X. Zhang, A. Brozena, J. Zheng, M. N. Garaga, B. H. Ko, Y. Mao, S. He, Y. Gao, P. Wang, M. Tyagi, F. Jiao, R. Briber, P. Albertus, C. Wang, S. Greenbaum, Y.-Y. Hu, A. Isogai, M. Winter, K. Xu, Y. Qi, L. Hu, *Nature* **2021**, *598*, 590.
[21] Y. Lin, M. Wu, J. Sun, L. Zhang, Q. Jian, T. Zhao, *Adv. Energy Mater.* **2021**, *11*, 2101612.
[22] Y. Ma, J. Wan, Y. Yang, Y. Ye, X. Xiao, D. T. Boyle, W. Burke, Z. Huang, H. Chen, Y. Cui, Z. Yu, S. T. Oyakhire, Y. Cui, *Adv. Energy Mater.* **2022**, *12*, 2103720.
[23] a) Z. Wang, J. Sun, R. Liu, Z. Ba, J. Dong, Q. Zhang, X. Zhao, *Small* **2023**, *19*, 2303422; b) L. Han, Y. Liu, C. Liao, Y. Zhao, Y. Cao, Y. Kan, J. Zhu, Y. Hu, *Nano Energy* **2023**, *112*, 108448.
[24] Y. He, S. Chen, L. Nie, Z. Sun, X. Wu, W. Liu, *Nano Lett.* **2020**, *20*, 7136.
[25] D. Zhou, Y.-B. He, R. Liu, M. Liu, H. Du, B. Li, Q. Cai, Q.-H. Yang, F. Kang, *Adv. Energy Mater.* **2015**, *5*, 1500353.
[26] P.-J. Alarco, Y. Abu-Lebdeh, A. Abouimrane, M. Armand, *Nat. Mater.* **2004**, *3*, 476.
[27] H.-J. Ha, E.-H. Kil, Y. H. Kwon, J. Y. Kim, C. K. Lee, S.-Y. Lee, *Energy Environ. Sci.* **2012**, *5*, 6491.
[28] J. Wang, S. Guo, Z. Li, W. Kou, J. Zhu, J. Dang, Y. Zhang, W. Wu, *Chem. Eng. J.* **2022**, *450*, 137994.
[29] a) Q. Liu, L. Li, G. Liu, X. He, Y. Niu, G. Li, *J. Power Sources* **2024**, *592*, 233897; b) F. Zhang, Y. Sun, Z. Wang, D. Fu, J. Li, J. Hu, J. Xu, X. Wu, *ACS Appl. Mater. Interfaces* **2020**, *12*, 23774.
[30] a) J.-Y. Liang, X.-X. Zeng, X.-D. Zhang, T.-T. Zuo, M. Yan, Y.-X. Yin, J.-L. Shi, X.-W. Wu, Y.-G. Guo, L.-J. Wan, *J. Am. Chem. Soc.* **2019**, *141*, 9165; b) M. Yao, Q. Ruan, T. Yu, H. Zhang, S. Zhang, *Energy Storage Mater.* **2022**, *44*, 93.
[31] L. Wang, S. Xu, Z. Wang, E. Yang, W. Jiang, S. Zhang, X. Jian, F. Hu, *eScience* **2023**, *3*, 100090.
[32] a) X. Zheng, D. Xu, N. Fu, Z. Yang, *J. Energy Chem.* **2023**, *81*, 603; b) Z. Shen, J. Zhong, S. Jiang, W. Xie, S. Zhan, K. Lin, L. Zeng, H. Hu, G. Lin, Y. Lin, S. Sun, Z. Shi, *ACS Appl. Mater. Interfaces* **2022**, *14*, 41022.
[33] H. Peng, T. Long, J. Peng, H. Chen, L. Ji, H. Sun, L. Huang, S.-G. Sun, *Adv. Energy Mater.* **2024**, 2400428.
[34] Y. Wang, L. Wu, Z. Lin, M. Tang, P. Ding, X. Guo, Z. Zhang, S. Liu, B. Wang, X. Yin, Z. Chen, K. Amine, H. Yu, *Nano Energy* **2022**, *96*, 107105.
[35] D. Lin, W. Liu, Y. Liu, H. R. Lee, P.-C. Hsu, K. Liu, Y. Cui, *Nano Lett.* **2016**, *16*, 459.
[36] S. Chen, L. Nie, X. Hu, Y. Zhang, Y. Zhang, Y. Yu, W. Liu, *Adv. Mater.* **2022**, *34*, 2200430.
[37] a) W. Zha, W. Li, Y. Ruan, J. Wang, Z. Wen, *Energy Storage Mater.* **2021**, *36*, 171; b) T. Zheng, X. Cui, Y. Chu, H. Li, Q. Pan, *ACS Appl. Mater. Interfaces* **2022**, *14*, 5932; c) W. Zha, J. Li, W. Li, C. Sun, Z. Wen, *Chem. Eng. J.* **2021**, *406*, 126754; d) H. Wang, Q. Wang, X. Cao, Y. He, K. Wu, J. Yang, H. Zhou, W. Liu, X. Sun, *Adv. Mater.* **2020**, *32*, 2001259; e) X. Zuo, Y. Cheng, L. Xu, R. Chen, F. Liu, H. Zhang, L. Mai, *Energy Storage Mater.* **2022**, *46*, 570; f) Y. Gong, C. Wang, M. Xin, S. Chen, P. Xu, D. Li, J. Liu, Y. Wang, H. Xie, X. Sun, Y. Liu, *Nano Energy* **2024**, *119*, 109054; g) B. Wang, G. Wang, P. He, L.-Z. Fan, *J. Membr. Sci.* **2022**, *642*, 119952; h) J. Sun, C. He, Y. Li, Q. Zhang, C. Hou, M. De Volder, K. Li, H. Wang, *Energy Storage Mater.* **2023**, *54*, 40; i) Y. Liu, P. Wang, Z. Yang, L. Wang, Z. Li, C. Liu, B. Liu, Z. Sun, H. Pei, Z. Lv, W. Hu, Y. Lu, G. Zhu, *Adv. Mater.* **2024**, 2400970; j) Z. Wang, L. Shen, S. Deng, P. Cui, X. Yao, *Adv. Mater.* **2021**, *33*, 2100353; k) K. Liu, H. Cheng, Z. Wang, Y. Zhao, Y. Lv, L. Shi, X. Cai, Z. Cheng, H. Zhang, S. Yuan, *Adv. Energy Mater.* **2024**, *14*, 2303940.
[38] J. Bae, Y. Qian, Y. Li, X. Zhou, J. B. Goodenough, G. Yu, *Energy Environ. Sci.* **2019**, *12*, 3319.
[39] J. Pokharel, A. Cresce, B. Pant, M. Y. Yang, A. Gurung, W. He, A. Baniya, B. S. Lamsal, Z. Yang, S. Gent, X. Xian, Y. Cao, W. A. Goddard, K. Xu, Y. Zhou, *Nat. Commun.* **2024**, *15*, 3085.
[40] a) S. Zou, Y. Yang, J. Wang, X. Zhou, X. Wan, M. Zhu, J. Liu, *Energy Environ. Sci.* **2024**, https://doi.org/10.1039/D4EE00822G; b) Q. Liu, L. Wang, X. He, *Adv. Energy Mater.* **2023**, *13*, 2300798.

 